Non-reciprocal voltage-current and impedance gyration effects in

ferrite/piezoelectric toroidal magnetoelectric composites

Jitao Zhang^{1†}, Bingfeng Ge¹, Qingfang Zhang¹, D. A. Filippov², Jie Wu¹, Jiagui Tao³, Zicheng Jia¹, Liying Jiang¹, Lingzhi Cao¹ and Gopalan Srinivasan⁴

A compact, efficient and passive magnetoelectric (ME) gyrator consisting of toroidal ferrite/piezoelectric composite and coil was developed, and its non-reciprocal V-I/I-V and bidirectional impedance conversion properties were systemically characterized. Maximum V/I coefficient of 115V/A over R_L >10k Ω was obtained for DME configuration and then the output power reaches its maximum of 2.59 μ W for optimum R_L =65 Ω under constant input density of 48.4 μ W/cm³, inversely I/V coefficient and then output power reach their maximum to 1.4mA/V and 0.83 μ W under optimum R_L =260 Ω and constant input of 32.3 μ W/cm³, respectively. Correspondingly, resistance-controlled capacitive/inductance tunabilities of 31pF/ Ω and 0.37 μ H/ Ω were achieved. Compared with traditional rectangular ME gyrators, the toroidal one has desired EMI tolerances due to its lower shape-induced anisotropy, near-zero demagnetization effects and closed magnetic circuit. These findings provided more flexibility of the device design for efficient and compact power electronics deployed in circumstances where the lower EMI at higher frequencies were required.

Power electronic devices that violate reciprocity, such as isolators, circulators and gyrators, are of use in versatile applications including high-power wireless transmitters, simultaneous-transmit-receive radar, full-duplex wireless radios and quantum computing implementations.^{1,2} As the fundamental circuit components or modules, voltage-current (V-I) and current-voltage (I-V) converters featured non-reciprocal metrics can be deployed in the cases of electrical isolating, impedance matching and power conversion.^{3,4} In general, the *V-I/I-V* converters were constructed by the high-gain, DC-biased operational amplifiers so that external power supply or battery was required to maintain normal operations. Nevertheless, conventional V-I/I-V converters are bulky and consumption and their deployments tend to be restricted to scenarios that fulfill the bidirectional and passive requirements. Thus, the flexibility of the converters was restricted by unidirectional V-I/I-V conversions. In view of these, efficient V-I/I-V converters with passive, bidirectional and non-reciprocal features are highly desired.

In 1948, Tellegen conjectured an ideal non-reciprocal gyrator as the fifth fundamental circuit element followed by resistors, capacitors, inductors and transformers, which enables any arbitrary non-reciprocal circuit with other four reciprocal elements integrated.⁵ Specifically, an example of inverting capacitive circuit behavior inductively would be the substitution of inductor with gyrators and easily integrated capacitors. More importantly, the possibility to implement gyrator prototype has

1

.

¹College of Electrical and Information Engineering, Zhengzhou University of Light Industry, Zhengzhou 450002, China

²Institute of Electronic and Information Systems, Novgorod State University, Veliky Novgorod 173003, Russia

³State Grid of Jiangsu Electric Power Co., Ltd. Nanjing 210024, China

⁴Physics Department, Oakland University, Rochester, Michigan 48309, USA

[†] Corresponding author: Tel. /Fax: +86 371 86601601. E-mail address: zhangjitao@zzuli.edu.cn (J. T. Zhang)

the potentials to revolutionize practical applications, and the implementation provides likely candidates for conventional V-I/I-V converters substitution. Shortly after, practical gyrator was first made by using of the Faraday rotation in pieces of ferrite placed in the waveguide. Until 2000s, ME materials and emergent multi-functional devices enriched the various realization pathways for the gyrator feasibilities, 8-12 and then the ME laminate with coil wound around it constituted the classical gyrator structure with capabilities of efficient V-I/I-V direct conversion. ¹³ Zhai et al. pioneered a bidirectional ideal ME gyrator with preferred gyration characteristics in Terfenol-D/PZT laminate, which offers considerably improved or simplified solutions to complex network topologies as well as an equivalent circuit theory to predict the *I-V* conversion. ¹⁴ Since 2016, the study on ME gyrators has been reinvigorated due to the advancements in scalable, integratable and efficient solid-state devices launched by DARPA MATRIX. 15-17 Meanwhile, modeling efforts were also developed by a set of nonlinear constitutive equations to direct device design and optimization. Focused efforts so far were devoted to improving power conversion efficiency by means of structural optimization, materials selection and energy dissipation reduction etc., and this enhancement can be achieved in the assistance of optimum resistance loaded, magnetic field biased and resonance frequency driving. 18-23 In despite of some of the end applications of ME gyrators have been successfully exploited including isolators, converters and circulators, 24-26 but for some special cases of high power density power conversions where the lower electromagnetic interference (EMI) at high frequency is needed, magnetic field emission and mutual couplings from open-loop ME gyrators can disturb nearby circuits, leading to increasingly severe EMI constraints in their environment.

In this study, a 4-wire 2-port toroidal ME gyrator consisting of strictly concentric ferrites/piezoelectric composite with toroidal coil wound around it was fabricated and developed, and the tri-layer toroidal composite operating in *C-C* mode was synthesized from circumferential magnetized nickel-zinc ferrite and transversely polarized PbaS-4 piezoelectric ceramics. In addition, bidirectional *V-I/I-V* conversion and impedance gyration effects of the presented ME gyrator were systemically characterized. To appreciate the toroidal structure employed, efficient *V-I/I-V* conversions with favorable EMI tolerances was satisfied due to inherent unique properties including lower shape-induced anisotropy, near-zero demagnetization effects, closed magnetic circuit, less magnetic leakage and high-frequency noise repression relative to its counterparts.

Polycrystalline nickel-zinc ferrite cylinder with composition of Ni_{0.8}Zn_{0.2}Sm_{0.02}Fe_{1.98}O₄ (NZSFO) was synthesized by conventional solid-state method,²⁷ and light samarium doping was intended to improve the dynamic magneto-mechanical conversion while decrease the hysteresis losses. 28,29 Sintered ferrite cylinder was sliced into thin discs with 14mm in diameter and 1mm in thickness by a low-frequency diamond saw (MTI Corp., Model SYJ-160, USA) and then magnetized in the circumference direction. Commercially purchased piezoelectric ceramic of PbaS-4 disc with similar dimensions were selected due to its high mechanical quality factor (~2200) (Yuhai Electronic Ceramics Co., Ltd, Zibo, China), and the electrodes were introduced from its two surfaces. Toroidal ME sample operating in C-C mode was fabricated with ferrite and PbaS-4 discs bonding together by epoxy resin adhesive (Vishay M-Bond 600 kit) and then cured at 120° C for 2h, followed by a round hole drilling with 8mm in diameter to keep strict concentricity. Finally, the hollow composite was wound by an enameled copper wire with diameter in 0.2mm to provide a toroidal solenoid of ~90 turns per arc. For the sample characterizations, non-reciprocal V-I/I-V gyration effects were measured using a lock-in amplifier (Zurich Model MFLI-500kHz), and impedance spectrum traces were captured by an impedance analyzer (Keysight Model E4990A). X-ray diffraction (XRD) was measured by X-ray diffractometer (Bruker Model Advance D8), and the magnetic properties were

measured by Physical Property Measurement System (PPMS-VSM, Quantum Design Model XL-7).

Desired spinel structure of ferrites was confirmed by XRD patterns as illustrated in Fig.1(a), and the emerging positions and relative intensities essentially complied with the standard XRD pattern in Fe₃O₄ (PDF#75-0449). Nevertheless, the presence of secondary phase Fe₂O₃ (PDF#25-1402) can be also observed in inconspicuous peaks with weak intensities, exhibiting that the light samarium doping can reduce the sintering temperature and directly hinder the phase formation, resulting in a reduction of crystallite size as well as the crystallinity of spinel NiZn ferrite phase.^{30,31} Characterizations of magnetic properties were carried out for rectangular NZSFO platelet with dimensions of 3mm×2mm×1mm to minimize the influences of demagnetization effects. As illustrated in Fig. 1(b), representative data of M vs H profile was obtained for in-plane fields parallel to the length of the rectangular platelet with a vibrating sample magnetometer (VSM), and favorable soft magnetic characteristics were achieved with remnant magnetization M_r =39emu/g and coercive field H_c =10Oe, respectively.

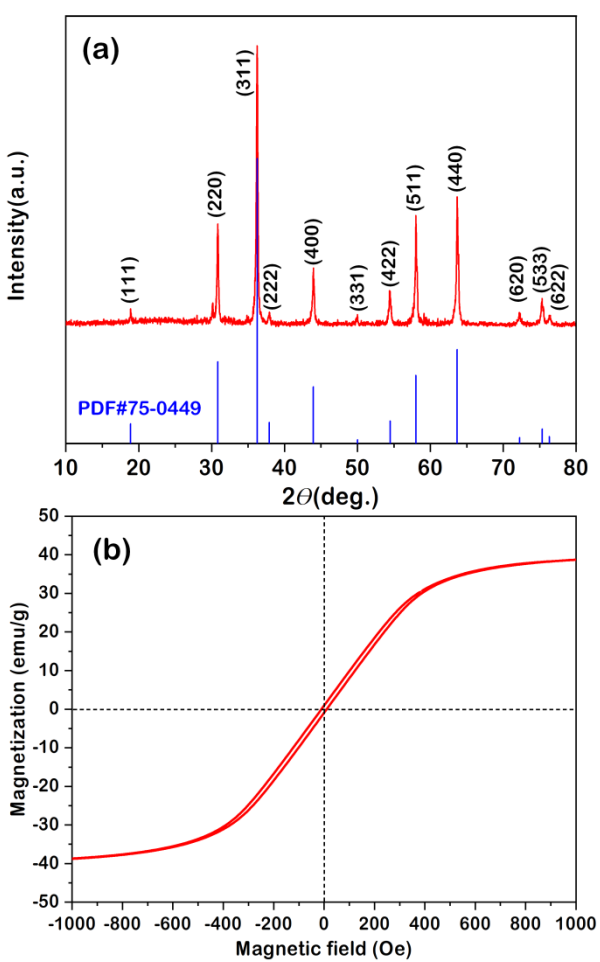


FIG.1. (a) XRD pattern of the sintered polyscrystalline Ni_{0.8} Zn_{0.2} Sm_{0.02}Fe_{1.98} O₄ platelet with standard results of Fe₃O₄ for comparison; (b)In-plane magnetic hysteresis loop for Ni_{0.8}Zn_{0.2}Sm_{0.02}Fe_{1.98}O₄ platelet

Generally, packaging a core transducer device implantable in a living shell so as to provide protection and bracing of the sensor device is dispensable for transducer manufactures, an electrical conductor of the sensor device should be sealed in an insulating substrate extending between proximal and distal ends.³² In this regard, presented toroidal ME transducer was caged in a non-magnetic fixture shell to avoid unexpected attenuation of capacitance induced by tight windings around it, which enables free vibrating of ferrites along circumferential directions. Beneficial results shown in Fig. 2 will suffice to illustrate how the fixture shell can facilitate the output performance,

and the inset shows schematic diagram and photograph of the packaged toroidal ME gyrator. Resonance dispersion of capacitance spectrum was captured in the range of 105kHz-115kHz for the naked toroidal sample with its resonance and anti-resonance peaks of 23.3nF. By contrast, an approximately 40% decrease in capacitance to 15nF was observed with packaged fixture shell, exhibiting that the winding carrier has great effects on the output of the toroidal samples. Moreover, the capacitance spectrum was employed to estimate the required optimum load resistance of ME gyrator by $R_{opt}=1/\omega C$. Specifically, e.g. for a measured capacitance of 15.01nF at EMR frequency of 109.118kHz, the required optimum load was predicted to be 97 Ω for the required external load to extract the maximum output power.

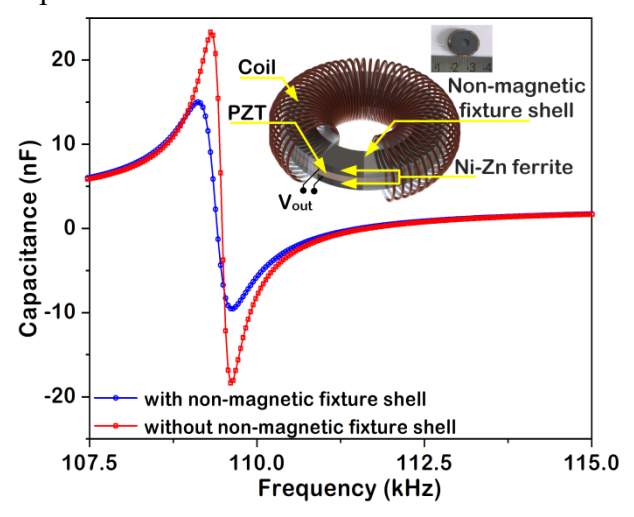


FIG.2. Capacitance traces of the toroidal ME gyrator with/without non-magnetic fixture shell over the range of 105kHz-115kHz for comparison. The inset shows schematic diagram and photograph of presented toroidal ME gyrator

Since the gyration effects were inspired by strain-mediated ME couplings along circumferential directions in toroidal composites, one would expect orders of magnitude stronger ME voltage coefficient (MEVC) when the frequency of the AC field is tuned to electromechanical resonance (EMR) frequency than that at the off-resonance frequencies. The frequency *f* dependence of MEVC was measured for the samples without DC biased and the typical MEVC vs *f* profile was shown in Fig. 3, MEVC reaches its maximum of 68.97V/cm Oe at EMR of 111.27 kHz, and then levels off at 973mV/cm Oe for higher *f*. The inset shows the FEM simulation image of circular magnetic field distribution inside the toroidal coil. Compared with the rectangular schemes, a closed circular AC magnetic field was imposed on the toroidal ferrites, prominent metrics of lower shape-induced anisotropy and near-zero demagnetization effects were introduced to obtain favorable *V-I/I-V* gyration effects.

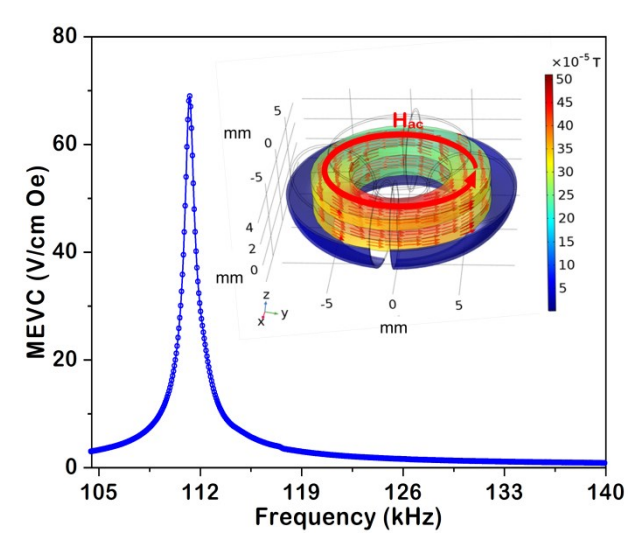


FIG.3. Resonance ME responses with frequency sweeping in the range of 105kHz-140kHz for toroidal ME gyrator. The inset shows simulation image of circular magnetic field distribution inside the toroidal coil.

The ME gyrator is a linear two port device which couples the current on one port to the voltage on the other or vice versa, and thus capability of direct V-I/I-V conversion characterized to evaluate the performance of ME gyrator. Figure 4 shows V-I/I-V ratio spectrum for the toroidal ME gyrator under various R_L of 50Ω , 200Ω , 500Ω , $1k\Omega$ and $2k\Omega$ over the frequency range of 105-125kHz, respectively. Clearly, a series of I-V ratio curves representing direct ME effects (DME) can essentially track the MEVC vs f profile, the selected representative I-V curves increase from 10V/A to 70V/A corresponding to R_L over 50Ω -2k Ω and the slight shifting of f_r , this observation can also be found in other heterostructure of Terfenol-D/PMN-PT composite.³³ As illustrated in Fig. 4(a), the inset shows R_L dependence of direct output power of P_{out} and I-Vratio under constant input power density of $48.4\mu\text{W/cm}^3$, respectively. Output P_{out} increases initially with increasing R_L and reaches its maximum of 2.59 μ W for optimum R_L =65 Ω , which matches with foregoing calculated value well. Further increase in R_L leads to a decrease in the magnitude of P_{out} and it approaches zero when R_L attains higher value of $R_L > 10 \text{k}\Omega$. Meanwhile, I-V ratio increases slowly with R_L over 50Ω -15k Ω and then levels off at 115V/A. Similar representative data on V-I vs f profiles under various R_L were obtained and shown in Fig. 4(b), representing converse ME effects (CME) the V-I ratio decreases precipitously with initial maximum of 1.4mA/V for the increasing R_L and then levels off at 0.1mA/V for R_L >8k Ω , while in this case the output power from the coil P_{out} reaches its maximum of $0.83\mu W$ for optimum $R_L=260\Omega$ under constant input power density of 32.3μ W/cm³. These *I-V/V-I* conversion ratios under EMR are ~33 times higher than that in the off-resonance region with facilitation of matched resistance load. Therefore, toroidal ME gyrators with bidirectional V-I/I-V non-reciprocity offer an alternative for V-I/I-V converters realization by well-matched load.

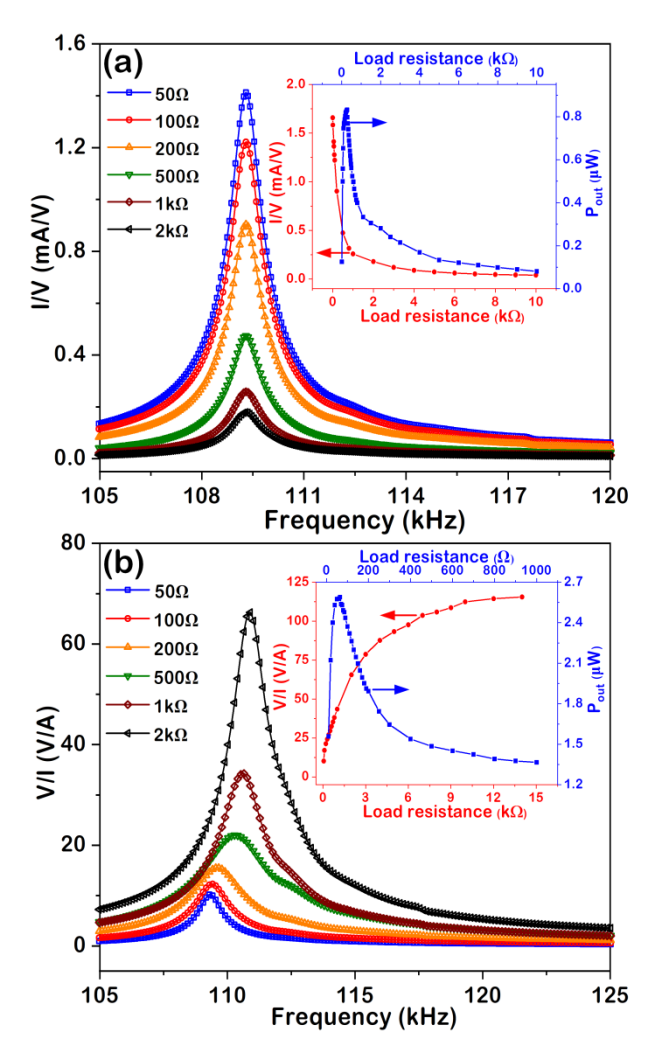


FIG.4 (a) I-V conversion ratio of the toroidal ME gyrator under various R_L in the frequency range of 105–125 kHz. The inset shows P_{out} and V/I as a function of R_L for toroidal ME gyrator, respectively; (b)Inversely, V-I conversion ratio of the toroidal ME gyrator under various R_L in the frequency range of 105–120 kHz. The inset shows P_{out} and I/V as a function of R_L , respectively.

An important property of the gyrator is that it directly inverts the V-I/I-V characteristics of a two-port electrical component or network accompanying the impedance converted for the linear ideal case, which enables a capacitive circuit behave inductively or vice versa for application in filter design and miniaturization.^{34,35} For the toroidal ME gyrator operating in DME configuration, capacitance C from piezoelectric port with load resistance R_L parallelly connected is equivalent to a RC oscillating network, and thus its impedance |Z| will change by variable R_L . In this case, measured C and |Z| spectrum under various R_L varied from 50Ω to $2k\Omega$ for toroidal ME gyrator were showed in Figs. 5(a)-(b), |Z| as well as C increases with R_L under resonance over the range of 100kHz-120kHz. Coupling factor T_{R-C} defined in Ref. 30 was employed to discribe the resistance controlled capacitive behaves quantitatively. In this regard, a value of $T_{R-C}=31 \text{pF}/\Omega$ was achieved around EMR frequency. Correspondingly, measurements of L and |Z| spectrum were implemented by parallel connecting R_L the coil port with its value varied from 50Ω to $2k\Omega$, and the results were depicted in Figs. 5(c)-(d). Coincidentally, no matter L or |Z| also shows an increasing tendency with load resistance but there is no resonance appeared, we infer from the results that this discrepancy is mainly attributed to the emerging rosonance determined by inferent natures of toroidal ME samples when the core ME transducer serves as output port in gyrators. As a result, a value of $T_{R-L}=0.37\mu H/\Omega$ was found to

discribe the resistance controlled inductive behaves quantitatively. The advances of these extended resistance-controlled inductance/capacitance characterictics of the ME gyrator are making the implementation and flexibility of efficient power electronics possible.

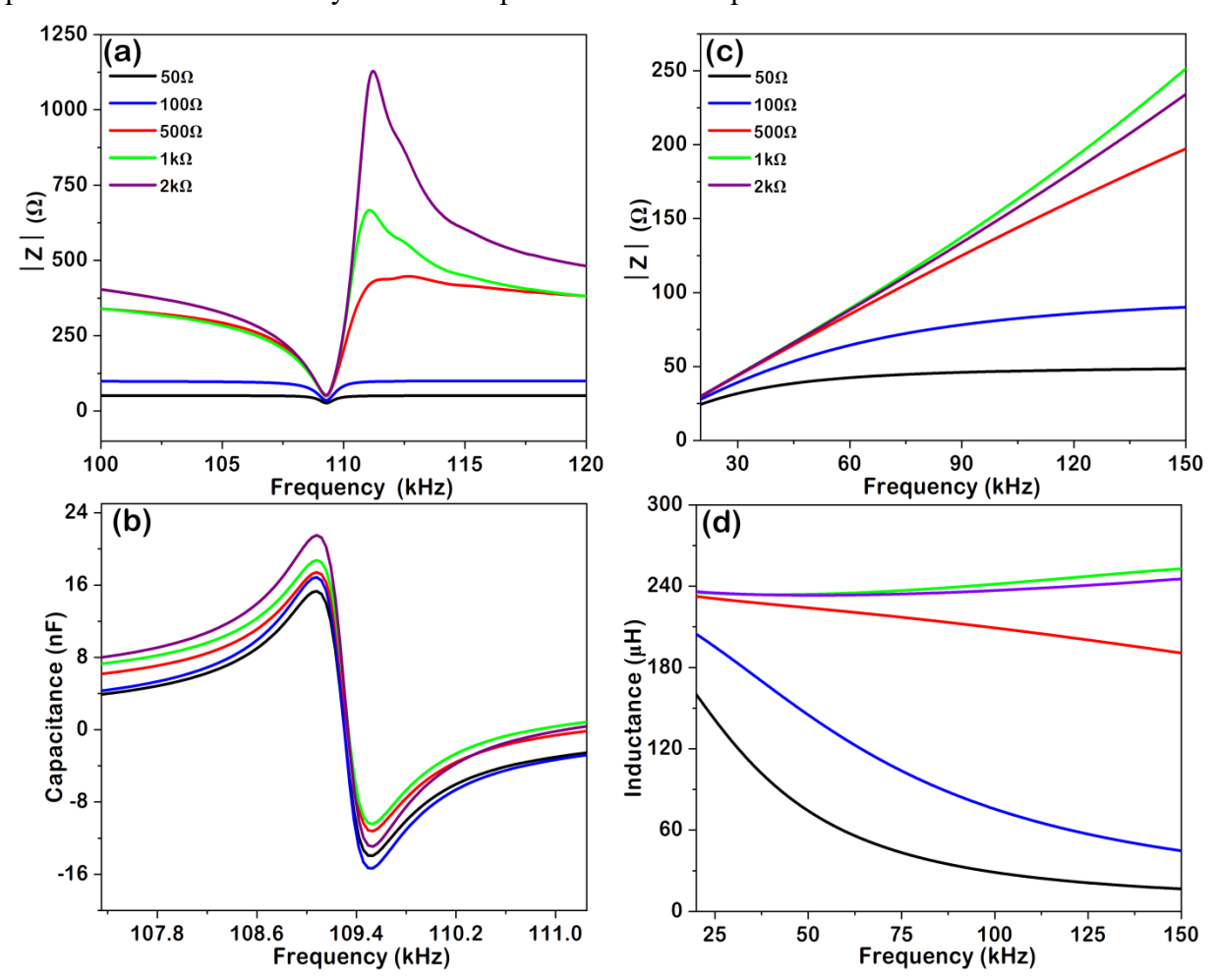


FIG 5(a) Impedance |Z| spectrum of the toroidal ME gyrator under various R_L connected to the ME port operating in DME case over the frequency range of 100-120 kHz; (b) Capacitance C spectrum of the toroidal ME gyrator under various R_L connected to the ME port over the frequency range of 100kHz-120 kHz; (c) Inversely, impedance |Z| spectrum of the toroidal ME gyrator under various R_L connected to the coil port operating in CME case over the frequency range of 15kHz-150kHz; (d) inductance L spectrum of the toroidal ME gyrator under various R_L connected to the coil port operating in CME case over the frequency range of 15kHz-150kHz

In summary, a tri-layer toroidal ME gyrator consisting of circumferential magnetized nickel-zinc ferrite and transversely polarized PbaS-4 with coil wound around it was fabricated and developed, and its ME response, V-I/I-V conversion and impedance gyration effects under EMR were systemically characterized. Under excitation of AC toroidal magnetic field, maximum MEVC of 68.97V/cm Oe was obtained at EMR of 111.27 kHz. In addition, value of V/I=115V/A over R_L > $10\text{k}\Omega$ was achieved for DME configuration and then the output power reaches its maximum of $2.59\mu\text{W}$ for optimum R_L = 65Ω under constant input density of $48.4\mu\text{W/cm}^3$. Inversely, for the CME case the value of I/V=1.4mA/V was achieved and the corresponding output power reaches its maximum of $0.83\mu\text{W}$ for optimum R_L = 260Ω under constant input power density of $32.3\mu\text{W/cm}^3$. Capability of resistance-controlled capacitive behaves can be described by a coupling factor of T_{R-C} with value of $31\text{pF}/\Omega$ while resistance-controlled inductive behaves represented by T_{R-L} with value of

 $0.37\mu H/\Omega$. These findings enable the use of ME gyrator for compact and efficient power electronic devices, providing great promising applications where the lower EMI at high frequency is required.

This research was financially supported by National Natural Science Foundation of China (NSFC) (Grant Nos. 61973279, 62004177, 62073299), Program for Innovative Research Group (in Science and Technology) in University of Henan Province (No.20IRTSTHN017). The study at Russia was supported by the Russian Foundation for Basic Research (Grant No. 18-52-00021). The research at Oakland University was supported by a grant from the National Science Foundation (Grant No. DMR-1808892).

DATA AVAILABILITY

The data that support the findings of this study are available from the corresponding author upon reasonable request.

- ¹ A. Nagulu, N. Reiskarimian, and H. Krishnaswamy, Nat. Electron. 3, 241 (2020).
- ² A. Nagulu, T. Dinc, Z. C. Xiao, M. Tymchenko, D. L. Sounas, A. Alù, and H. Krishnaswamy, IEEE Trans. Microw. Theory. **66**, 4706 (2018).
- ³ J. Y. Zhu and F. Lyu, Energies **12**, 2261 (2019).
- ⁴ D. Z. Montanher, V. F. Freitas, D. M. Silva, F. J. Gaiotto, J. R. D. Pereira, L. F. Cotica, I. A. Santos, D. Garcia, J. A. Eiras, R. Guo, and A. S. Bhalla, Integr. Ferroelectr. **174**, 210 (2016).
- ⁵ B. D. H Tellegen, Philips Res **3**, 81 (1948).
- ⁶ Y. M. Jia, S. W. Or, H. L. W. Chan, J. Jiao, H. S. Luo, and S. van der Zwaag, Appl. Phys. Lett. **94**, 263504 (2009).
- ⁷ C. L. Hogan, Bell. Sys. Tech. J **31**, 1 (1952).
- ⁸ N. A. Spaldin and R. Ramesh, Nat. Mater. 18, 203 (2019).
- ⁹ M. PourhosseiniAsl, X. Y. Gao, S. Kamalisiahroudi, Z. H. Yu, Z. Q. Chu, J. K. Yang, H. Y. Lee, and S. X. Dong, Nano Energy **70**, 104506 (2020).
- ¹⁰ Z. Q. Chu, M. PourhosseiniAsl, and S. X. Dong, J. Phys. D: Appl. Phys. **51**, 243001 (2018).
- ¹¹ J. T. Zhang, W. He, M. Zhang, H. M. Zhao, Q. Yang, S. T. Guo, X. L. Wang, X. W. Zheng, and L. Z. Cao, Rev. Sci. Instrum. 86, 095005 (2015).
- ¹² J. T. Zhang, D. Y. Chen, D. A. Filippov, K. Li, Q. F. Zhang, L. Y. Jiang, W. W. Zhu, L. Z. Cao, and G. Srinivasan, Appl. Phys. Lett. 113, 113502 (2018).
- ¹³ C. M. Leung, S. W. Or, F. F. Wang, and S. L. Ho, J. Appl. Phys. **109**, 104103 (2011).
- ¹⁴ J. Y. Zhai, J. F. Li, S. X. Dong, D. Viehland, and M. I. Bichurin, J. Appl. Phys. **100**, 124509 (2006).
- ¹⁵ C. M. Leung, X. Zhuang, D. Friedrichs, J. F. Li, R. W. Erickson, V. Laletin, M. Popov, G. Srinivasan, and D. Viehland, Appl. Phys. Lett. 111, 122904 (2017).
- ¹⁶ X. Zhuang, C. M. Leung, J. F. Li, and D. Viehland, Appl. Phys. Lett. 111, 103902 (2017).
- ¹⁷ X. Zhuang, C. M. Leung, G. Sreenivasulu, M. Gao, J. T. Zhang, G. Srinivasan, J. Li, and D. Viehland, Appl. Phys. Lett. **111**, 163902 (2017).
- ¹⁸ J. T. Zhang, W. W. Zhu, D. A. Filippov, W. He, D. Y. Chen, K. Li, S. T. Geng, Q. F. Zhang, L. Y. Jiang, L. Z. Cao, R. Timilsina, and G. Srinivasan, Rev. Sci. Instrum. 90, 015004 (2019).
- ¹⁹ C. M. Leung, X. Zhuang, M. Gao, X. Tang, J. R. Xu, J. F. Li, J. T. Zhang, G. Srinivasan, and D. Viehland, Appl. Phys. Lett. 111, 182901 (2017).
- ²⁰ C. M. Leung, G Sreenivasulu, X. Zhuang, M. Gao, X. Tang, J. R. Xu, J. F. Li, G Srinivasan, and D Viehland, Appl. Phys. Lett. **112**, 242901 (2018).
- ²¹ X. Zhuang, C. M. Leung, J. F. Li, and D. Viehland, Sensors **20**, 3332 (2020).

- ²² X. Zhuang, C. M. Leung, J. F. Li, G. Srinivasan, and D. Viehland, IEEE Trans. Ind. Electron. 66, 2499 (2019).
- ²³ X. L. Qian, S. Lin, G. Cheng, X. W. Yao, H. L. Ren, and W. Wang, Remote. Sens. 12, 143 (2020).
- ²⁴ S. Bosco, F. Haupt, and D. P. DiVincenzo, Phys. Rev. Appl. 7, 024030 (2017).
- ²⁵ C. Tu, C. Z. Dong, Z. Q. Chu, H. H. Chen, X. F. Liang, and N. X. Sun, Appl. Phys. Lett. 113, 262904 (2018).
- ²⁶ S. Y. Zhang, M. J. Zhang, and S. W. Or, IEEE Trans. Magn **52**, 4002405 (2016).
- ²⁷ J. T. Zhang, W. W. Zhu, D. Y. Chen, H. W. Qu, P. Zhou, M. Popov, L. Y. Jiang, L. Z. Cao, and G. Srinivasan, J. Magn. Magn. Mater. 473, 131 (2019).
- ²⁸ A. C. F. M. Costa, A. P. A. Diniz, A. G. B. De Melo, R. H. G. A. Kiminami, D. R. Cornejo, A. A. Costa, and L. Gama, J. Magn. Magn. Mater. 320, 742 (2008).
- ²⁹ J. T. Zhang, D. Y. Chen, K. Li, D. A. Filippov, B. F. Ge, Q. F. Zhang, X. X. Hang, L. Z. Cao, and G. Srinivasan, AIP. Adv. 9, 035137 (2019).
- ³⁰ A. C. F. M. Costa, M. R. Morelli, and R. H. G. A. Kiminami, J. Mater. Sci. **39**, 1773 (2004).
- ³¹ K. Tanbir, M. P. Ghosh, R. K. Singh, M. Kar, and S. Mukherjee, J. Mater. Sci. Mater. El. 31, 435 (2020).
- 32 D. T. H. Giang, D. X. Dang, N. X. Toan, N. V. Tuan, A. T. Phung, and N. H. Duc, Rev. Sci. Instrum. 88, 015004 (2017).
- ³³ Y. J. Wang, X. Y. Zhao, J. Jiao, L. H. Liu, W. N. Di, H. S. Luo, and S. W. Or, J. Alloys. Compd. **500**, 224 (2010).
- ³⁴ C. M. Leung, X. Zhuang, J. R. Xu, G. Srinivasan, J. F. Li, and D. Viehland, Appl. Phys. Lett. 109, 202907 (2016).
- 35 C. M. Leung, X. Zhuang, J. Xu, J. Li, J. T. Zhang, G. Srinivasan, and D. Viehland, AIP. Adv. 8, 055803 (2018).